

# RSC Advances

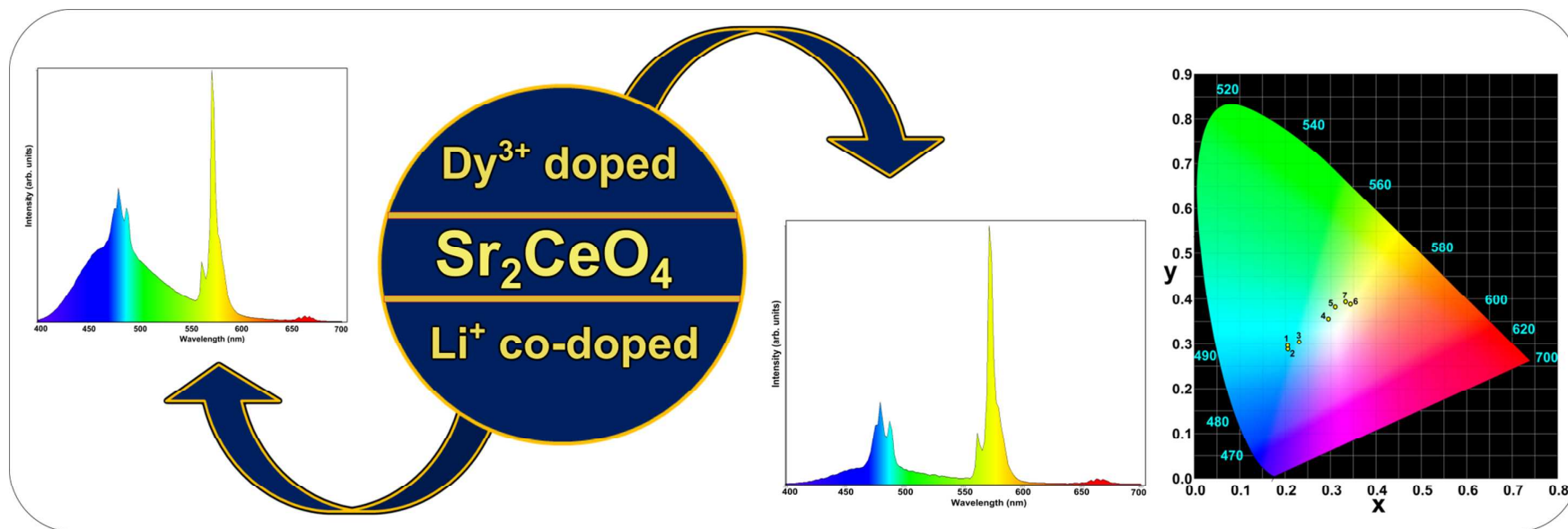


This is an *Accepted Manuscript*, which has been through the Royal Society of Chemistry peer review process and has been accepted for publication.

*Accepted Manuscripts* are published online shortly after acceptance, before technical editing, formatting and proof reading. Using this free service, authors can make their results available to the community, in citable form, before we publish the edited article. This *Accepted Manuscript* will be replaced by the edited, formatted and paginated article as soon as this is available.

You can find more information about *Accepted Manuscripts* in the [Information for Authors](#).

Please note that technical editing may introduce minor changes to the text and/or graphics, which may alter content. The journal's standard [Terms & Conditions](#) and the [Ethical guidelines](#) still apply. In no event shall the Royal Society of Chemistry be held responsible for any errors or omissions in this *Accepted Manuscript* or any consequences arising from the use of any information it contains.



## Synthesis and photoluminescence properties of novel $\text{Sr}_2\text{CeO}_4:\text{Dy}^{3+}$ nanophosphor with enhanced brightness by $\text{Li}^+$ co-doping

D. L. Monika<sup>a</sup>, H. Nagabhushana<sup>a\*</sup>, R. Hari Krishna<sup>b\*</sup>, B. M. Nagabhushana<sup>b</sup>,  
S. C. Sharma<sup>c</sup>, Tiju Thomas<sup>d</sup>

<sup>a</sup>Prof. C.N.R. Rao Centre for Nano Research, Tumkur University, Tumkur 572103, India

<sup>b</sup>Department of Chemistry, M. S. Ramaiah Institute of Technology, Bangalore 560054, India

<sup>c</sup>Chhattisgarh Swami Vivekanand Technical University, Bhilai-493441, India

<sup>d</sup>Materials Research Centre, Indian Institute of Science, Bangalore 560 012, India

### Abstract

A series of  $\text{Dy}^{3+}$  (0.005-0.09 mol%) and  $\text{Li}^+$  (0.005-0.03 mol%) co-doped strontium cerate ( $\text{Sr}_2\text{CeO}_4$ ) nanopowders are synthesized by low temperature solution combustion synthesis. The effects of  $\text{Li}^+$  doping on the crystal structure, chemical composition, surface morphology and photoluminescence properties are investigated. The X-ray diffraction results confirm that all the samples calcined at 900 °C show pure orthorhombic (Pbam) phase. Scanning electron microscopy analysis reveals that particles adopt irregular morphology and porous nature of the product. Room temperature photoluminescence results indicate that the phosphor can be effectively excited by near UV radiation (290 to 390 nm) which results in the blue (484 nm) and yellow (575 nm) emission. Furthermore, PL emission intensity and wavelength are highly dependent on the concentration of  $\text{Li}^+$  doping. The emission intensity is enhanced by ~3 folds with  $\text{Li}^+$  doping. White light is achieved by merely varying dopant concentration. The colour purity of the phosphor is confirmed by CIE co-ordinates ( $x=0.298$ ,  $y=0.360$ ). The study demonstrates a simple and efficient method for the synthesis of novel nanophosphors with enhanced white emission.

**Keywords:** nanophosphor, solution combustion, photoluminescence, energy transfer, CIE

---

\*Corresponding author: *E-mail*: rhk.chem@gmail.com (R. Hari Krishna) bhushanvlc@gmail.com

(H. Nagabhushana); Mobile. No: +91 9886434109

## 1. Introduction

Over the last decade extensive attention has been given to the research areas related to white light emission due to their potential application in modern lighting systems. These systems are preferred replacements for classical incandescent and fluorescent lamps, due to their high efficiencies.<sup>1-3</sup> The most widely used method to fabricate white light emitting devices (LEDs) involves the use of phosphors as light transducers to convert near-ultraviolet (NUV) or blue light to white light.<sup>4-6</sup> NUV phosphor converted LEDs are preferred in several applications due to their excellent optical stability, high color tolerance and high conversion efficiency.<sup>7-9</sup> Therefore, phosphors that are efficiently excited by near-UV light are desirable.

Rare earth (RE) elements when doped into a suitable inorganic host can act as an effective luminophore. In fact RE doped phosphors based light emitting devices have already been used in various applications.<sup>3-6</sup> Rare earths act as efficient emitters both in trivalent and divalent states owing to inner f-f and f-d transitions respectively. This fact has been explored in order to engineer the absorption and emission spectrum of practical phosphors.<sup>10</sup> Generally, the trivalent rare earth ions like  $\text{Eu}^{3+}$ ,  $\text{Sm}^{3+}$  and  $\text{Dy}^{3+}$  having f-f transitions result in sharp emission peaks, since the electron-lattice interaction is very weak for inner electrons. Whereas f-d transitions of divalent rare earth ions such as  $\text{Eu}^{2+}$  results in broad emission peak. This is due to the participation of the d-electrons in chemical bonding. It may be noted that in divalent RE ions, the  $(4f)^n$  to  $(4f)^{n-1}(5d)^1$  transitions involve the promotion of a single electron from the 4f orbitals to an empty 5d orbital.<sup>11-12</sup>

Phosphors employing trivalent Dysprosium ions ( $\text{Dy}^{3+}$ ) have been widely studied due to the potential applications in white light emission. This is because  $\text{Dy}^{3+}$  has intense blue (484 nm) and yellow (575 nm) emission lines.<sup>13-16</sup> However these  $\text{Dy}^{3+}$  transitions are very sensitive to the chemical environment surrounding the luminophore. Hence, the ratios of the two emission bands are different in different hosts. Therefore, it is possible to modulate the emitted light by suitably choosing host or varying the composition of the host, for the

realization of white light emission.<sup>15-17</sup> Hence the choice of host is an important criterion to harness the rich luminescence characteristics of the Dy<sup>3+</sup> luminophore.

Among the inorganic hosts studied so far, oxide-based phosphors have received the most attention due to their ease of synthesis, stability, and the nontoxic nature.<sup>17-21</sup> Therefore oxide-based phosphors are likely to emerge as a preferred choice for making display devices and solid state lighting. Danielson et al.<sup>22</sup> have reported a novel blue luminescent material Sr<sub>2</sub>CeO<sub>4</sub>, prepared using a combinatorial material synthesis technique. Since then, Sr<sub>2</sub>CeO<sub>4</sub> has attracted much attention of the researchers due to several advantages, like lack of radioactive elements, non-toxicity, higher chemical and thermal stability.<sup>23-25</sup> Apart from these advantages, Sr<sub>2</sub>CeO<sub>4</sub> also possesses some desirable qualities such as (i) ligands-to-metal charge transfer (CT) transition of Ce<sup>4+</sup> at ~340 nm, (ii) efficient energy transfer that can occur from the Ce<sup>4+</sup>-O<sup>2-</sup> CT state to the trivalent rare earth in Sr<sub>2</sub>CeO<sub>4</sub>:RE<sup>3+</sup>,<sup>23</sup> (iii) high efficiency for absorbing UV radiation and (iv) the large band gap and covalent bond energy prove its capability for using as a phosphor material.<sup>24</sup> The Sr<sub>2</sub>CeO<sub>4</sub> blue luminescence is believed to originate from a ligand-to-metal (O<sup>2-</sup>→Ce<sup>4+</sup>) charge transfer mechanism. This process occurs between the lower coordination number terminal oxygen atoms associated with the low dimensional structure, in combination with an adjacent Ce<sup>4+</sup> centre in Sr<sub>2</sub>CeO<sub>4</sub> structure. The emission is fairly broad (FWHM ~ 3821 cm<sup>-1</sup>) at the blue region (450–500 nm), which makes this material a potential candidate for phosphor applications.<sup>23-26</sup>

Recent research reports reveal that the doping of RE ions along with the alkali metal ions (Li<sup>+</sup>, K<sup>+</sup> and Na<sup>+</sup>) emerged as an effective way to enhance the photoluminescence (PL) brightness and emission characteristics of the nanophosphors.<sup>27-30</sup> With the removal of the charge unbalance problem with a less defective crystal structure, alkali metal ions not only enhance the efficiency of trivalent RE ions, but also play a crucial role to control emission colors of phosphor materials. This technique has been employed on several systems, like

CaMO<sub>4</sub>:Dy<sup>3+</sup>,<sup>27</sup> Y<sub>2</sub>Zr<sub>2</sub>O<sub>7</sub>:Dy<sup>3+</sup>,<sup>28</sup> YBO<sub>3</sub>:Eu<sup>3+</sup>,<sup>29</sup> YPO<sub>4</sub>:Eu<sup>3+</sup>,<sup>30</sup> etc. to achieve impressive luminescence properties. But so far, to the best of our knowledge, there are no studies on the white light emission from Sr<sub>2</sub>CeO<sub>4</sub>: Dy<sup>3+</sup> nanophosphors with Li<sup>+</sup> co-doping. In this paper we report the tuning of white light in Sr<sub>2</sub>CeO<sub>4</sub>: Dy<sup>3+</sup>, Li<sup>+</sup> nanophosphor synthesized by solution combustion route. Here we also report the quality of white light using CIE coordinates and correlated color temperature (CCT).

## 2. Experimental

### 2.1 Materials and synthesis

All the chemicals used are of analytical grade purity, and are used without further purification. Strontium nitrate (Sr(NO<sub>3</sub>)<sub>2</sub>·9H<sub>2</sub>O; 99.99%, Merck Ltd.), Cerium nitrate (Ce(NO<sub>3</sub>)<sub>2</sub>·6H<sub>2</sub>O; 99.99%, Sigma Aldrich Ltd.) and Dysprosium nitrate (Dy(NO<sub>3</sub>)<sub>3</sub>·6H<sub>2</sub>O; 99.99%, Sigma Aldrich Ltd.) are mixed in suitable stoichiometric ratios to get products with chemical formula Sr<sub>2-x</sub>Dy<sub>x</sub>CeO<sub>4</sub> (x=0.005-0.09). Oxalydihydrazide (C<sub>2</sub>H<sub>6</sub>N<sub>4</sub>O<sub>2</sub>) is prepared by using hydrazine hydrate and diethyloxalate as reported in the literature<sup>31</sup> and is used as fuel.

The fuel:oxidizer ratio is calculated based on oxidizing and reducing valencies of the reactants by setting F/O=1, as reported in our earlier report.<sup>32</sup> An aqueous solution containing stoichiometric amounts of reactants is taken in a cylindrical pyrex petri dish of approximately 300 ml capacity and introduced into a muffle furnace maintained at a temperature of 500 ±10 °C. The reaction mixture undergoes thermal dehydration and auto-ignites with liberation of gaseous products such as oxides of nitrogen and carbon.<sup>31</sup> The combustion flame propagates throughout the reaction mixture. The heat of reaction is sufficient for the decomposition of the redox mixture and to form the desired product. The whole process is completed in less than 5 min and a highly porous white Sr<sub>2</sub>CeO<sub>4</sub>:Dy<sup>3+</sup> nanopowders were obtained. Similar procedure is followed to prepare different concentrations of Li<sup>+</sup> co-doped Sr<sub>2-x</sub>Dy<sub>x</sub>CeO<sub>4</sub>

( $x=0.075$ ,  $y=0.005$  to  $0.03$ ) phosphors, (Lithium nitrate ( $\text{Li}(\text{NO}_3)$ , 99.99%, Merck Ltd. is used as source of  $\text{Li}^+$ ). All the samples after synthesis are calcined at  $900^\circ\text{C}$  for 3 h to improve the crystallinity.

## 2.2 Characterization

The powder X-ray diffraction studies are carried out using Shimadzu 7000 powder X-ray diffractometer with  $\text{Cu K}_\alpha$  radiation ( $\lambda=1.541 \text{ \AA}$ ). Fourier Transform Infra-red spectroscopy (FTIR) spectrum is taken using a Perkin-Elmer Rx1 instrument. The morphology and structure of the samples are inspected using a Hitachi-3000 scanning electron microscope (SEM). For performing SEM, a layer of Au is deposited on the samples using a sputtering deposition set up. This is necessary to get clear SEM images since the samples are insulating. Transmission electron microscopy (TEM) analysis and High resolution TEM (HRTEM) are performed on a Hitachi H-8100 (accelerating voltage up to 200 kV,  $\text{LaB}_6$  filament) equipped with energy dispersive spectroscopy (EDS) (Kevex Sigma TM Quasar, USA). The photoluminescence (PL) measurements are carried out using a Jobin Yvon spectrofluorometer (Fluorolog-3, HORIBA) equipped with a 450-W xenon lamp as the excitation source.

## 3 Results and Discussion

### 3.1 Powder X-ray diffraction analysis (PXRD)

Fig. 1 and Fig. 2 shows the XRD patterns of  $\text{Sr}_2\text{CeO}_4:\text{Dy}^{3+}$  and  $\text{Sr}_2\text{CeO}_4:\text{Dy}^{3+}:\text{Li}^+$  nanoparticles. The XRD patterns fits well with the orthorhombic crystal structure with JCPDS 50-0511 with Pbam space group. No additional peaks for other phases have been found in both the patterns of  $\text{Sr}_{2-x}\text{CeO}_4:\text{Dy}_x$  and  $\text{Sr}_{2-y}\text{Dy}_x\text{Li}_y\text{CeO}_4$ . This indicates that dopants ions were effectively doped into the  $\text{Sr}_2\text{CeO}_4$  host lattices. Since the ionic radii of  $\text{Sr}^{2+}$  and  $\text{Li}^+$  are 0.072 nm and 0.068 nm (for octahedral co-ordination) respectively,  $\text{Li}^+$  easily

substitutes  $\text{Sr}^{2+}$  in the  $\text{Sr}_2\text{CeO}_4$  lattice. However, a careful observation of the XRD patterns in Fig. 2(b) reveals that peaks are shifted slightly towards higher  $2\theta$  values with the increase in concentration of  $\text{Li}^+$ . Shrinking of unit cell caused due to the substitution of larger  $\text{Sr}^{2+}$  by smaller  $\text{Li}^+$  is responsible for this higher angle shift. It is interesting to note that in contrast with the other XRD peaks, when  $\text{Li}^+$  concentration is  $x=0.03$ , the pattern shifts towards lower angle. The difference in the peak shift to higher/lower angle can be explained as follows. When the concentration of  $\text{Li}^+$  ions is below  $x=0.03$ ,  $\text{Li}^+$  ions occupy substitutional sites ( $\text{Sr}^{2+}$ ). However, when  $x>0.07$ , of  $\text{Li}^+$  ions begin to take interstitial sites resulting in the host lattice expansion. Hence beyond a critical co-doping concentration, the trends in the peak shift reverses. The calculated values of the lattice parameter (a), crystallite size (D) and FWHM of the (130) peak are presented in Table 1. The crystallite size of all the synthesized samples lies within the range 19-27 nm, which confirms the formation of  $\text{Sr}_2\text{CeO}_4$  crystals in the nanosized region. With Li incorporation, we observe a reduction in the FWHM, and a concomitant increase in the sharpness of the (130) peak. This indicates that  $\text{Li}^+$  acts as a self-promoting agent for the enhanced crystallization of the lattice.<sup>33</sup>

### 3.2 Scanning electron microscopy (SEM)

SEM micrographs of  $\text{Sr}_2\text{CeO}_4:\text{Dy}^{3+}$  and  $\text{Li}^+$  co-doped  $\text{Sr}_2\text{CeO}_4:\text{Dy}^{3+}$ , nanophosphors are shown in Fig. 3(a,b) and (c,d) respectively. It is observed from the micrographs that some bigger agglomerates are spherical, but the primary particles are irregular in shape. Agglomerates made of these irregular particles range in size between few microns to a few tens of microns. Minimization of surface energy is the most likely reason for this observed agglomeration of nanoparticle.<sup>34</sup> Typical of combustion derived products, all the samples exhibit large number of pores and voids in their structure. This can be attributed to large amount of gases escaping out of the reaction mixture during the combustion.<sup>35</sup> Interestingly in

all the samples some agglomerates as assume spherical shape of varying sizes (~1-3  $\mu\text{m}$ ), which is very unusual for combustion derived products.

### 3.3 Fourier transform infrared spectroscopy (FTIR)

In order to confirm the phase formation and purity of the samples, FTIR analysis is carried out. Fig. 4(a) and 4(b) shows the FTIR spectra of  $\text{Sr}_2\text{CeO}_4: \text{Dy}^{3+}$ , and  $\text{Sr}_2\text{CeO}_4: \text{Dy}^{3+}, \text{Li}^+$  nanophosphor respectively. The dominant band corresponding to  $\text{CO}_3^{2-}$  from the precursor appeared around  $1457 \text{ cm}^{-1}$  in all the products. On the other hand, the peak at  $3465 \text{ cm}^{-1}$  is attributed to the physically adsorbed  $\text{H}_2\text{O}$ .<sup>36</sup> Bands ranging from  $400\text{-}900 \text{ cm}^{-1}$  originates from stretching and bending modes of metal–oxygen (M–O) groups. Two distinct bands were observed at  $440$  and  $861 \text{ cm}^{-1}$  which originates from stretching vibrations of Ce–O in octahedral coordination state ( $\text{CeO}_6$  octahedral units).<sup>37</sup> Since there is no discernible change in the position of peaks, it is reasonable to believe that the dopant has occupied the position of  $\text{Sr}^{2+}$  ions in crystal.

### 3.4 Transmission electron microscopy (TEM)

Transmission electron microscopy (TEM) is carried out on the  $\text{Sr}_2\text{CeO}_4: \text{Dy}^{3+}, \text{Li}^+$  nanophosphor samples. TEM, selected area electron diffraction pattern (SAED) and high-resolution TEM (HRTEM) micrographs of the nanophosphor are shown in Fig. 5(a–c). Fig. 5a clearly indicates that the particles are nearly spherical and elongated with diameters ~10 nm. In addition, we can observe some larger particles with diameters ~30 nm. Typical of combustion derived products, all the particles are highly agglomerated. The diffraction pattern (Fig. 5b) revealed a polycrystalline composition with four clearly distinguishable spotty but fully closed rings, which are indexed according to the  $\text{Sr}_2\text{CeO}_4$  orthorhombic structure. The lattice fringe observed (Fig. 5c) correspond to an interplanar distance of 0.3 nm; this is comparable to the interplanar distance of the (130) plane planes in  $\text{Sr}_2\text{CeO}_4$ .<sup>22</sup>

### 3.5 Photoluminescence studies (PL)

The photoluminescence characteristics of the  $\text{Sr}_2\text{CeO}_4: \text{Dy}^{3+}$  and  $\text{Li}^+$  co-doped  $\text{Sr}_2\text{CeO}_4: \text{Dy}^{3+}$  nanophosphors are investigated by PL excitation and emission spectra. PL excitation spectra of  $\text{Sr}_{2-x}\text{Dy}_x\text{CeO}_4$  ( $x=0.005-0.09$ ) and  $\text{Sr}_{1.9925-y}\text{Li}_y\text{CeO}_4$  ( $y=0.005-0.03$ ) nanophosphors are shown in Fig. 6(a) and 6(b). This excitation spectrum is recorded by monitoring the emission of  $\text{Dy}^{3+}$  at 575 nm. The excitation spectra consist of broad bands and some sharp narrow peaks. The broad bands consist of two peaks centred at 290 and 340 nm; this is attributed to the charge transfer band (CTB) caused by an electron transfer from the  $\text{O}^{2-}$  ( $2p$ ) orbital to the empty states of the  $4f^6$  configuration of  $\text{Ce}^{4+}$  ( $\text{Ce}^{4+}-\text{O}^{2-}$  transition).<sup>38</sup> The peak at 290 nm originated due to transition from terminal oxygen ( $\text{O}_t$ ) to  $\text{Ce}^{4+}$ . The peak at 340 nm is ascribed to transition from equatorial oxygen ( $\text{O}$ ) to  $\text{Ce}^{4+}$ .<sup>38</sup> Apart from this broad CTB, the excitation spectra contain several other sharp peaks observable in the longer wavelength region between 350 to 480 nm. These sharp features are due to intra-configuration  $f-f$  transitions of the  $\text{Dy}^{3+}$  dopant ions. In general, the direct excitation of the  $\text{Dy}^{3+}$  ground state to the higher levels in the  $4f$  configuration results in the electronic transitions ( ${}^6\text{H}_{15/2} \rightarrow {}^6\text{P}_{3/2}$ ) at 326 nm, ( ${}^6\text{H}_{15/2} \rightarrow {}^6\text{P}_{7/2}$ ) at 352 nm, ( ${}^6\text{H}_{15/2} \rightarrow {}^6\text{P}_{5/2}$ ) at 366 nm, ( ${}^6\text{H}_{15/2} \rightarrow {}^4\text{I}_{13/2}$ ) at 385 nm, ( ${}^6\text{H}_{15/2} \rightarrow {}^4\text{G}_{11/2}$ ) at 424 nm, ( ${}^6\text{H}_{15/2} \rightarrow {}^4\text{I}_{15/2}$ ) at 453 nm and ( ${}^6\text{H}_{15/2} \rightarrow {}^4\text{F}_{9/2}$ ) at 475 nm.<sup>39</sup> However we could observe sharp peaks only at 385 and 424 nm. This might be because the other expected peaks (expected at 326, 352 and 366 nm) are buried within the broad CTB of host lattice.

Photoluminescence emission spectra of the  $\text{Sr}_{2-x}\text{Dy}_x\text{CeO}_4$  ( $x=0.005-0.09$ ) and  $\text{Sr}_{1.9925-y}\text{Dy}_{0.0075}\text{Li}_y\text{CeO}_4$  ( $y=0.005-0.03$ ) nanophosphors, excited by 424 nm wavelength, are shown in Fig. 7(a) and 7(b), respectively. The emission spectra of all the phosphors ( $\text{Sr}_2\text{CeO}_4: \text{Dy}^{3+}$  and  $\text{Li}^+$  co-doped  $\text{Sr}_2\text{CeO}_4: \text{Dy}^{3+}$ ) consist of a broad band ranging from 400 to 500 nm corresponding to host emission. Along with this host emission there is overlap of

Dy<sup>3+</sup> emission at 488 nm. Besides this there is a prominent emission peak at 575 nm, and a weak feature is observed at 662 nm. The emission peaks of Dy<sup>3+</sup> at 488 nm, 575 nm and 662 nm can be assigned to the transitions from the <sup>4</sup>F<sub>9/2</sub> to the <sup>6</sup>H<sub>15/2</sub>, <sup>6</sup>H<sub>13/2</sub> and <sup>6</sup>H<sub>11/2</sub> states, respectively.<sup>37</sup> Among these emissions, the yellow band (575 nm) and the blue band (488 nm) are the predominant transitions. It is well known that <sup>4</sup>F<sub>9/2</sub> → <sup>6</sup>H<sub>15/2</sub> lines originate from magnetic dipole transitions, while the <sup>4</sup>F<sub>9/2</sub> → <sup>6</sup>H<sub>3/2</sub> lines originate from electric dipole transitions. The magnetic dipole transition is independent of the symmetry and the site occupied by Dy<sup>3+</sup> ions in the host. But the electric dipole transition is very sensitive to the crystal field, and the emission intensity is strongly affected by the site symmetry of the dopant ion.<sup>40</sup> The site symmetry of Dy<sup>3+</sup> can be determined by taking the ratio of emission intensities of both magnetic dipole and electric dipole transition (i.e. I<sub>575</sub>/I<sub>488</sub>). In the emission spectrum of Dy<sup>3+</sup> ions, the yellow emission (<sup>4</sup>F<sub>9/2</sub> → <sup>6</sup>H<sub>13/2</sub>) is often dominant when the Dy<sup>3+</sup> ion is located in the low symmetry local site without inversion center and the blue emission (<sup>4</sup>F<sub>9/2</sub> → <sup>6</sup>H<sub>15/2</sub>) is stronger than yellow one when it is located at a high-symmetry local site with an inversion center.<sup>41,42</sup> Fig.8. shows the plot of ratio of transition intensities with dopant concentration. The value is found to decrease with increasing dopant concentration. This indicates that the Dy<sup>3+</sup> located in the low symmetry local site without inversion center.<sup>43</sup>

In order to investigate the difference in emission spectra resulting from various excitations, the PL emission spectra of Sr<sub>2</sub>CeO<sub>4</sub>: Dy<sup>3+</sup> and Li<sup>+</sup> co-doped Sr<sub>2</sub>CeO<sub>4</sub>: Dy<sup>3+</sup> was recorded at 290 nm (host excitation) and 424 nm (direct excitation). Fig. 9 shows emission spectra upon excitation at 290 nm. It can be seen that the emission spectra have the similar properties to that of samples excited at 424 nm except for variation in PL intensities. This is true for all Sr<sub>2</sub>CeO<sub>4</sub>: Dy<sup>3+</sup> and Li<sup>+</sup> co-doped Sr<sub>2</sub>CeO<sub>4</sub>: Dy<sup>3+</sup> with different doping concentrations. Additionally, it is worth noting that in the PL emission spectra the broad blue emission band due to the host emission decreases with the increase of Dy<sup>3+</sup> doping

concentration. This is indicating energy transfer from the host to the  $\text{Dy}^{3+}$  ions as dopant content increases. This clearly indicates that  $\text{Sr}_2\text{CeO}_4$  is a very efficient host for  $\text{Dy}^{3+}$ .

Fig.10 is the schematic energy-level diagram showing the excitation and emission mechanism of  $\text{Sr}_2\text{CeO}_4:\text{Dy}^{3+}$  phosphors. Upon host excitation at 290 nm, the photon energy is absorbed by host leading to the charge transfer of  $\text{O}^{2-} \rightarrow \text{Ce}^{4+}$ ; this energy is transferred to 4f shell of  $\text{Dy}^{3+}$ . Thus the electrons of  $\text{Dy}^{3+}$  at  $^4\text{F}_{9/2}$  excited state can populate both from non-radiative charge transfer feeding and non-radiative transitions from higher excited states. Then the characteristic emissions at 488, 575 and 662 nm correspond to the  $^4\text{F}_{9/2} \rightarrow ^6\text{H}_j$  ( $j = 15/2, 13/2, 11/2$ ) transitions, respectively.<sup>16</sup> While the direct excitation of  $\text{Dy}^{3+}$  ions inducing the transitions from ground state to the metastable excited states. Part of the excited electrons in these metastable excited levels are repopulated into  $^4\text{F}_{9/2}$  level by the multiphonon assisted non-radiative transitions. The transitions from  $^4\text{F}_{9/2}$  to  $^6\text{H}_j$  ( $j = 15/2, 13/2, 11/2$ ) are radiative and produce the emission lines of 488, 575 and 662 nm, respectively.

Fig. 11(a) and 11(b) shows the variation of PL intensity with  $\text{Dy}^{3+}$ , and  $\text{Li}^+$  co-doped  $\text{Sr}_2\text{CeO}_4$  nanophosphors respectively. It can be seen, upon excitation at 290 nm and 424 nm, the Intensity (I) Vs dopant (x) curves shows similar trend. That is the emission intensity initially increases quickly with  $\text{Dy}^{3+}$  doping concentration and reaches a maximum value at  $x=0.0075$ ; subsequently it decreases due to the concentration quenching. It is found that for both host excitation and direct excitation the optimum  $\text{Li}^+$  concentration is  $y=0.01$  for a fixed  $\text{Dy}^{3+}$  concentration,  $x=0.0075$ .

The type of interaction for concentration quenching can be estimated by Dexter theory.<sup>44</sup> The emission intensity per activator ion is given by the equation

$$\frac{1}{X} = \frac{K}{\left[1 + \beta(x)^{\frac{Q}{3}}\right]} \dots \dots \dots (3)$$

where  $x$  is the activator concentration,  $Q$  is the exchange interaction, where  $Q = 6, 8$  or  $10$  for electric dipole-dipole (D-D), electric dipole-quadrupole (D-Q), or electric quadrupole-quadrupole (Q-Q) interactions respectively.<sup>45</sup>  $K$  and  $\beta$  are the constants for a given host lattice. Fig. 12(a) and 12(b) shows the plot of  $\log [Dy^{3+}]$  Vs  $\log I/Dy^{3+}$  for excitation wavelength at 424 and 290 nm respectively. The trend of the graph at 350nm is found to be linear with the slope  $-1.849$ . Using Eq.5 the  $Q$  value obtained is 6 indicating dipole-dipole interactions is the key mechanism for the concentration quenching of  $Dy^{3+}$  emission in  $Sr_2CeO_4$  host. However, when the sample is excited at 290 nm the slope value obtained is  $-1.523$  where concentration quenching is due to energy transfer.

### 3.6 Influence of $Li^+$ co-doping: charge compensation

The evolution of the emission spectra after  $Li^+$  co-doping upon 280 nm and 350 nm are shown Fig. 7(b) and 9(b) respectively. For each sample,  $Dy^{3+}$  concentration is fixed at  $x = 0.0075$  and  $Li^+$  concentration is varied from  $x = 0.005$ - $0.03$ . As expected, co-doping  $Li^+$  does not have any influence on position of the emission peaks. However, the emission intensity of  $Sr_2CeO_4: Dy^{3+}, Li^+$  increases considerably when compared to the  $Sr_2CeO_4: Dy^{3+}$  nanophosphor. This improvement of PL emission intensity with  $Li^+$  codoping can be attributed to the charge compensation phenomenon.<sup>27, 28</sup>

The charge compensation demands removal of three  $Sr^{2+}$  ions to introduce two rare earth ( $RE^{3+}$ ) ions for effective lattice substitution, this might restrict the  $RE^{3+}$  concentration, causing an increase in concentration of cation vacancies.<sup>37</sup> Hence it becomes difficult to maintain the charge neutrality in the RE doped phosphors. General outer electronic configuration of alkali metals is  $ns^1$ , and they acquire mono-positive charge after losing their electron. Therefore, these alkali metals can be used for charge compensation in  $Dy^{3+}$  in  $Sr_2CeO_4$  phosphors. Charge compensation is achieved by replacing two  $Sr^{2+}$  ions by one  $Dy^{3+}$

and one  $\text{Li}^+$  ion. Lattice distortion and non-radiative transitions will appear if more  $\text{Li}^+$  ions are added, which reduces the emission intensity.

### 3.7 Commission Internationale de l'Eclairage (CIE) coordinates of $\text{Sr}_2\text{CeO}_4: \text{Dy}^{3+}, \text{Li}^+$ and $\text{Sr}_2\text{CeO}_4: \text{Dy}^{3+}$

For practical lighting applications, colour quality is specified in terms of 1931 CIE chromatic color coordinates. This scheme is based on the known spectral response of the human eye to the 3 primary colors: red, green and blue.<sup>46</sup> In general the colour of any light sources can be represented on the (x,y) coordinates in this colour space. These colour coordinates are one of the most important parameters for evaluating phosphors performance. Fig. 13 shows the CIE 1931 chromaticity diagram for  $\text{Sr}_2\text{CeO}_4: \text{Dy}^{3+}(x=0.005-0.09)$  phosphors. The calculated CIE color coordinates for all the samples are summarized in Fig. 13 (inset). As can be seen, all the samples fall into the scope of white light emission. Ideal white light with CIE (x, y) = (0.298, 0.360) and correlated color temperature CCT = 6896 K are realized when the concentration of  $\text{Dy}^{3+}$  (x=0.03). Hence this material shows promise for a white light source to meet the needs of the illustrated applications.

## 4 Conclusion:

We have successfully demonstrated a simple, low temperature energy saving route to synthesize  $\text{Dy}^{3+}$  doped and  $\text{Dy}^{3+}, \text{Li}^+$  co-doped  $\text{Sr}_2\text{CeO}_4$  nanophosphors. A wide range of  $\text{Dy}^{3+}$  and  $\text{Li}^+$  concentrations have been explored. The resulting nanophosphors exhibit a bright fluorescent yellow emission at 574 nm ( $^4\text{F}_{9/2} \rightarrow ^6\text{H}_{13/2}$ ) and blue emission at 488nm ( $^4\text{F}_{9/2} \rightarrow ^6\text{H}_{15/2}$ ). Furthermore, we have examined the comparative photoluminescence (PL) of the  $\text{Dy}^{3+}$  doped and  $\text{Dy}^{3+}\text{-Li}^+$  co-doped  $\text{Sr}_2\text{CeO}_4$  nanophosphors. These studies clearly show that  $\text{Li}^+$  co-doping enhances the emission intensity of the phosphors. Furthermore Li incorporation also improves the crystallinity of the phosphors. We suggest that the

luminescence improvement observed is due to charge compensation expected in systems with Li co-activators. White light emission was achieved by tuning yellow to blue ratio, which was done by varying the Dy<sup>3+</sup> dopant concentration. The quality of emitted white light was evaluated using CIE 1931 chromatic color coordinates.

### **Acknowledgement:**

DLM is grateful to the Management and Principal of *Shridevi Institute of Engineering & Technology, Tumkur*, for their constant support and encouragement.

### **References**

- [1] E. Pavitra, G. Seeta Rama Raju, Yeong Hwan Ko and Jae Su Yu, *Phys. Chem. Chem. Phys.*, 2012, **14**, 11296.
- [2] ZhiguoXia,Weiwei Wu, *Dalton Trans.*, 2013, **42**, 12989.
- [3] Xinguo Zhang, Menglian Gong, *Dalton Trans.*, 2014, **43**, 2465.
- [4] DonglingGeng, Mengmeng Shang, Yang Zhang, Hongzhou Lian, Ziyong Cheng, Jun Lin, *J. Mater. Chem. C*, 2013, **1**, 2345.
- [5] Linfeng Hu, Renzhi Ma, Tadashi C. Ozawa, Takayoshi Sasaki, *Inorg. Chem.* 2010, **49**, 2960.
- [6] Linfeng Hu, Renzhi Ma, Tadashi C. Ozawa, Fengxia Geng, Nobuo Iyi, Takayoshi Sasaki, *Chem. Commun.*, 2008, 4897.
- [7] Hak-Sung Jung, Young-Jae Kim, Shin-Woo Ha and Jin-KyuLee. *J. Mater.Chem. C*, 2013, **1**, 5879.
- [8] S. Nakamura, *The Blue Laser Diode: The Complete Story*, Springer, Berlin, NewYork, 2nd edn, 2000.

- [9] J. R. Oh, S.-H. Cho, Y.-H. Lee and Y. R. Do, *Electrochem. Solid- State Lett.*, 2010, **13**, J5.
- [10] W. M. Yen, S. Shionoya and H. Yamamoto, *Phosphor Handbook*, Taylor & Francis Group, LLC, 2nd edn, 2007.
- [11] R. Reisfeld, C. K. Jorgensen, In *Lasers and Excited States of Rare Earths*; Springer-Verlag: New York, 1993; p 93
- [12] M. Nogami, Y. Abe, *Appl. Phys. Lett.* 1996, **69** (25), 3776
- [13] M. R. N. Soares, M. J. Soares, A. J. S. Fernandes, L. Rino, F. M. Costa and T. Monteiro, *J. Mater. Chem.*, 2011, **21**, 15262.
- [14] Xiaohua Liu, Wendou Xiang, Fengming Chen, Zhengfa Hu, Wei Zhang, *Mater. Res. Bull.*, 2013, **48**, 281.
- [15] A.K. Ambast, J. Goutam, S. Som, S.K. Sharma, *Spectrochim. Acta, Part A*, 2014, **122**, 93.
- [16] Xianghong He, Weihua Li, Quanfa Zhou, *Mater. Sci. Eng., B* 2006, **134**, 59.
- [17] Xinghua Zhang, Zunming Lu, Fanbin Meng, Long Hu, Xuewen Xu, Jing Lin, Chengchun Tang, *Mat. Lett.*, 2012, **79**, 292.
- [18] E. Pavitra, G. Seeta Rama Raju, Wook Park and Jae Su Yu, *New J.Chem.*, 2014, **38**, 163.
- [19] R. Hari Krishna, B. M. Nagabhushana, H. Nagabhushana, N. Suriya Murthy, S. C. Sharma, C. Shivakumara, R. P. S. Chakradhar. *J. Phys. Chem. C*, 2013, **117** (4), 1915.
- [20] R. Hari Krishna, B.M. Nagabhushana, H. Nagabhushana, R.P.S. Chakradhar, R. Sivaramakrishna, C. Shivakumara, Tiju Thomas, *J Alloys Compd*, 2014, **585**, 129.
- [21] Satish Laxman Shinde, Karuna Kar Nanda, *CrystEngComm*, 2013, **15**, 1043.
- [22] E. Danielson, M. Devenney, D.M. Giaquinta, J.H. Golden, R.C. Haushalter, E.W. McFarland, D.M. Poojary, C.M. Reaves, W.H. Weinberg, X.D. Wu, *Science.*, 1998, **279**, 837.

- [23] Tomasz Grzyb, AgataSzczeszak, JustynaRozowska, Janina Legend ziewicz, Stefan Lis, *J. Phys. Chem. C.*, 2012,**116**, 3219.
- [24] Lili Shi, Hongjie Zhang, ChengyuLi, Qiang Su, *RSC Advances*, 2011, **1**, 298.
- [25] Takayuki Hirai and Yusuke Kawamura,*J. Phys. Chem. B* 2005, **109**, 5569
- [26] Wang Hay Kan and VenkataramanThangadurai, *Inorg. Chem.* 2012, **51**, 8973.
- [27] Guan Li , JiaGuoqi , Yang Baozhu , Li Xu , Jin Litao, Yang Zhiping, Fu Guangsheng, *J rare earths*, 2011, **29(6)**, 540.
- [28] QingqingDua, Guangjun Zhou, Juan Zhou, Xiao Jia, Haifeng Zhou, *J. Alloys Compds*, 2013,**552**,152.
- [29] Dong Woo Kim, R. Balakrishnaiah, SoungSoo Yi, KwangDuk Kim, Sung-Hoon Kim, Kiwan Jang, HoSueb Lee and Jung Hyun Jeong, *ECS Trans.* 2009, **16(30)**, 30, 13.
- [30] Zhang Lixin , Jiu Hongfang , Fu Yuehua , Sun Yixin , Wang Yuanzhong, *J rare earths*, 2013, **31(5)**, 449.
- [31] K. C Patil, M. S. Hegde, T. Rattan, S.T. Aruna, *Chemistry of Nanocrystalline Oxide materials*, World Scientific Press, Singapore, 2008.
- [32] Singanahally T. Aruna , Alexander S. Mukasyan, *Curr. Opin. Solid State Mater. Sci.*,2008, **12**, 44.
- [33] SubhajitSaha, Swati Das, Uttam Kumar Ghorai, NileshMazumder, Bipin Kumar Gupta and Kalyan Kumar Chattopadhyay, *Dalton Trans.*, 2013,**42**, 12965.
- [34] E. Shafia, A. Aghaei, A. Davarpanah, M. Bodaghi, M. Tahriri and S. H. Alavi *Trans. Ind. Ceram. Soc.*, 2011,**70 (2)**, 71.
- [35] J. J. Kingsley, K.C. Patil, *Mater. Lett.* 1988; **6**, 427.
- [36] K. Suresh, K. V. R. Murthy, Ch. AtchyuthaRao, N. V. PoornachandraRao, B. SubbaRao, *J. Lumin*, 2013, **133**, 96.
- [37] Abanti Nag, T. R. Narayanan Kutty, *J. Mater. Chem.*,2003, **13**, 370.

- [38] Jefferson L.Ferrari, AnaM.Pires ,OsvaldoA.Serra , MarianR.Davolos, J Lumin, 2011,**131**, 25.
- [39] A.K. Ambast, J. Goutam, S. Som, S.K. Sharma, Spectrochim. Acta, Part A, 2014, **122**, 93.
- [40] X. Liu, W. Xiang, F. Chen, Z. Hu, W. Zhang, Mater. Res. Bull., 2013,**48**, 281.
- [41]. Ch. Victory Devi, Ganggam Phaomei , N. Yaiphaba , N. Rajmuhon Singh, J. Alloys Compd. 2014, **583**, 259.
- [42]. N. Kiran, A. Suresh Kumar, J. Mol. Struct. 2013, **6-1**, 1054.
- [43]. M. Sundara Rao, V. Sudarsan, M.G. Brik, Y. Gandhi, K. Bhargavi, M. Piasecki, I.V. Kityk, N. Veeraiah, J. Alloys Compd. 2013, **575**, 375.
- [44] D. L. Dexter, J. Chem. Phys. 1953, **23**, 836.
- [45] L. G. Van Uitert, J. Electrochem. Soc., 1967, **114**, 1048.
- [46] Shionoya S, Yen W M. Phosphor Handbook, Phosphor Research Society, CRC Press, 1998, 459.

**Table Caption:**

Table.1. Estimated lattice parameter and particle size of  $\text{Sr}_{2-x}\text{Dy}_x\text{CeO}_4$  ( $x=0.0025-0.09$ ) and  $\text{Sr}_{1.9925-y}\text{Dy}_{0.0075}\text{Li}_y\text{CeO}_4$  ( $y=0.005-0.03$ ) nanophosphor.

**Figure Captions:**

Fig.1. XRD of  $\text{Sr}_{2-x}\text{Dy}_x\text{CeO}_4$  ( $x=0.0025-0.09$ ) nanophosphor.

Fig.2. (a) XRD patterns of  $\text{Sr}_{1.9925-y}\text{Dy}_{0.0075}\text{Li}_y\text{CeO}_4$  ( $y=0.005-0.03$ ) nanophosphor. (b) (130) peak shift patterns as Li concentration is increased.

Fig.3. SEM micrographs of (a, b)  $\text{Sr}_{2-x}\text{Dy}_x\text{CeO}_4$  ( $x=0.0075$ ) and (c, d)  $\text{Sr}_{1.9925-y}\text{Dy}_{0.0075}\text{Li}_y\text{CeO}_4$  ( $y=0.01$ ) nanophosphor.

Fig.4. FTIR spectra of (a)  $\text{Sr}_{1.9925}\text{Dy}_{0.0075}\text{CeO}_4$  and (b)  $\text{Sr}_{1.9925}\text{Dy}_{0.0075}\text{Li}_{0.01}\text{CeO}_4$  nanophosphor.

Fig.5. (a) TEM (b) HRTEM (c) SAED pattern of  $\text{Sr}_{1.9925}\text{Dy}_{0.0075}\text{CeO}_4$  nanophosphor.

Fig.6. PL excitation spectra of (a)  $\text{Sr}_{2-x}\text{Dy}_x\text{CeO}_4$  ( $x=0.0025-0.09$ ) and (b)  $\text{Sr}_{1.9925-y}\text{Dy}_{0.0075}\text{Li}_y\text{CeO}_4$  ( $y=0.005-0.03$ ) nanophosphor monitored at emission wavelength of 575 nm.

Fig.7. PL emission spectra of (a)  $\text{Sr}_{2-x}\text{Dy}_x\text{CeO}_4$  ( $x=0.0025-0.09$ ) and (b)  $\text{Sr}_{1.9925-y}\text{Dy}_{0.0075}\text{Li}_y\text{CeO}_4$  ( $y=0.005-0.03$ ) nanophosphor excited at 424 nm.

Fig.8. Variation of the relative intensities ( $I_R$ ) with  $\text{Dy}^{3+}$  concentrations.  $I_R$  is the ratio of the intensities of the 575 nm magnetic dipole transition line, and the 488 nm electric dipole transition line (i.e  $I_{575}/I_{488}$ )

Fig.9. PL emission spectra of (a)  $\text{Sr}_{2-x}\text{Dy}_x\text{CeO}_4$  ( $x=0.0025-0.09$ ) and (b)  $\text{Sr}_{1.9925-y}\text{Dy}_{0.0075}\text{Li}_y\text{CeO}_4$  ( $y=0.005-0.03$ ) nanophosphor excited at 290 nm.

Fig.10. Schematic diagram illustrating the energy and charge transfer pathways, and electronic transitions in  $\text{Sr}_{2-x}\text{Dy}_x\text{CeO}_4^+$ .

Fig.11. Emission intensity as a function of  $\text{Dy}^{3+}$  concentrations in  $\text{Sr}_{2-x}\text{Dy}_x\text{CeO}_4$  ( $x=0.0025-0.09$ ). Inset shows variation of emission intensity of  $\text{Sr}_{1.9825-y}\text{Dy}_{0.0075}\text{Li}_y\text{CeO}_4$  as a function of Li concentration ( $y=0.005-0.03$ ). The nanophosphor is monitored at both 290 and 424 nm excitation wavelengths.

Fig.12. Plot of  $\log[\text{Dy}^{3+}]$  vs.  $\log(I/[\text{Dy}^{3+}])$ . The slope of the straight line fit indicates that (a) dipole-dipole interaction, and (b) energy transfer are the causes for the concentration quenching in  $\text{Dy}^{3+}$  ions, when excitation wavelengths are 424 and 290 nm respectively.

Fig.13. CIE 1931 colour coordinates of  $\text{Sr}_{2-x}\text{Dy}_x\text{CeO}_4$  ( $x=0.0025-0.09$ ) nanophosphors as a function of  $x$ .

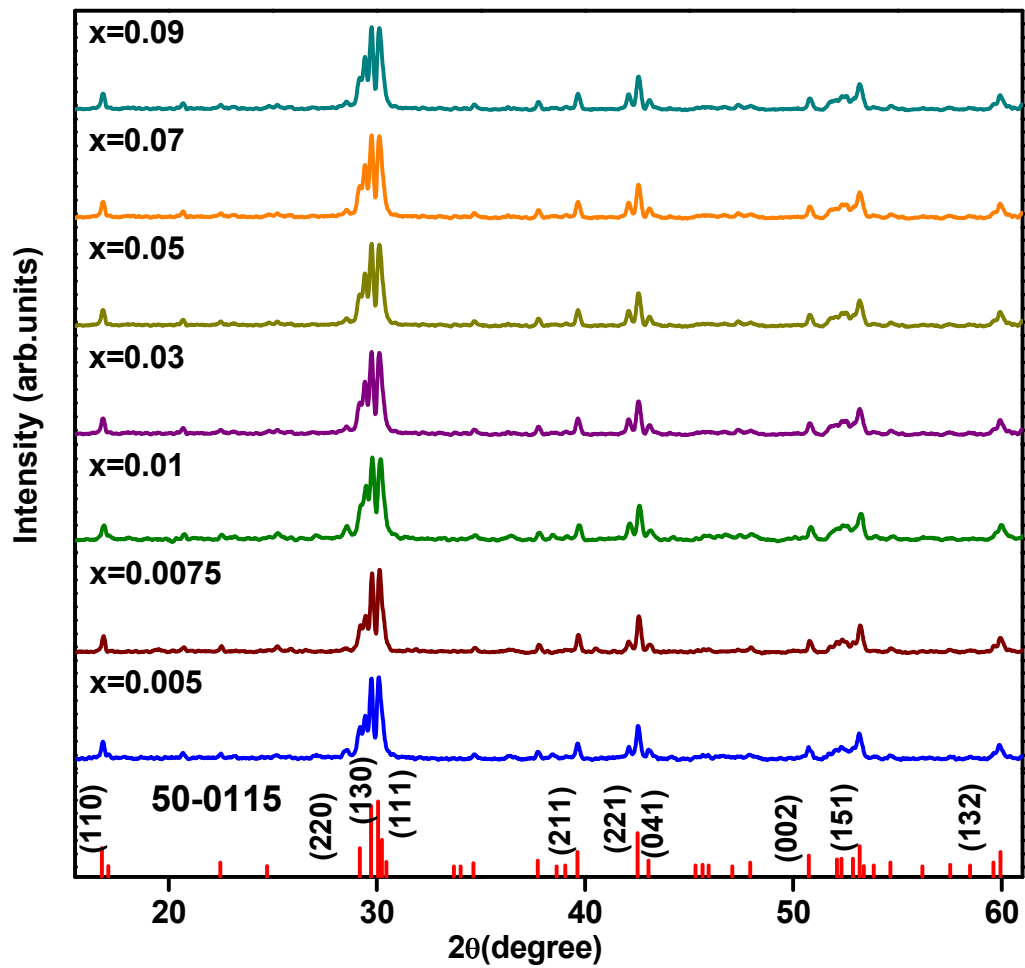


Fig. 1.

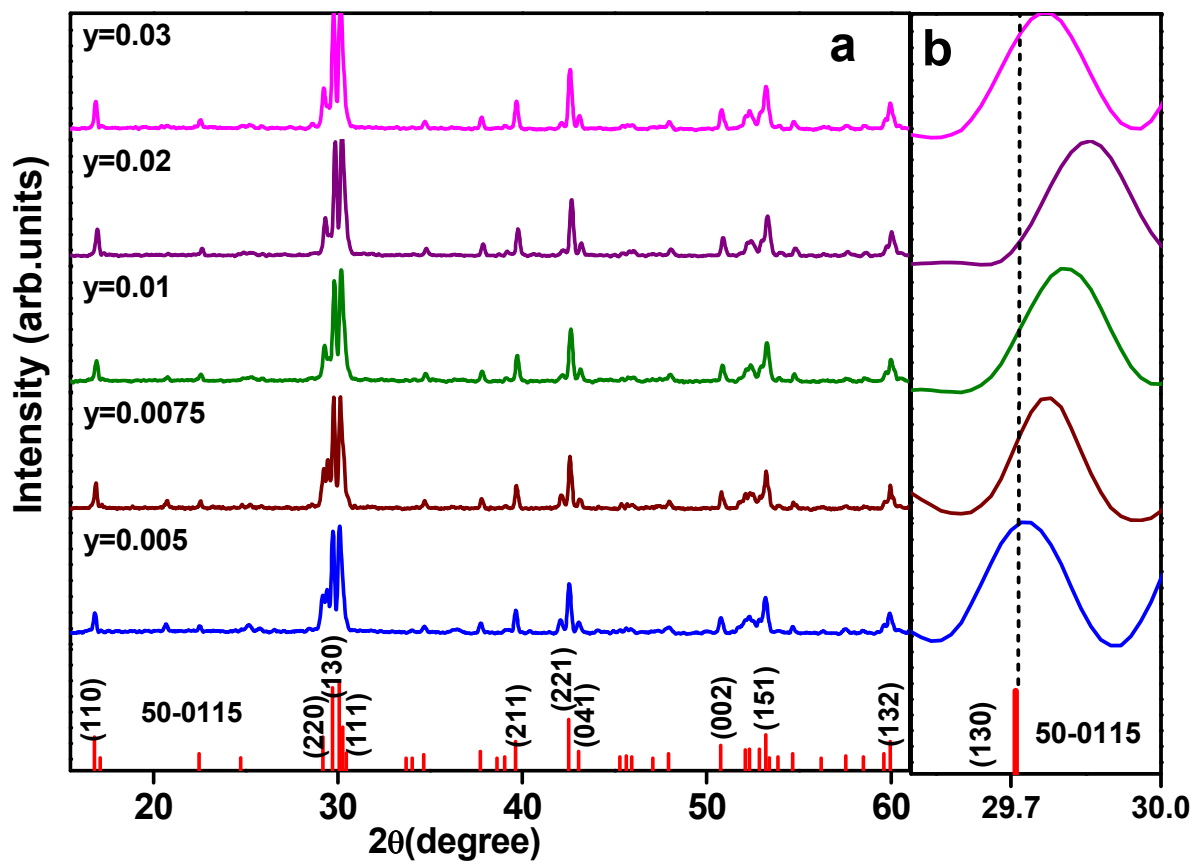
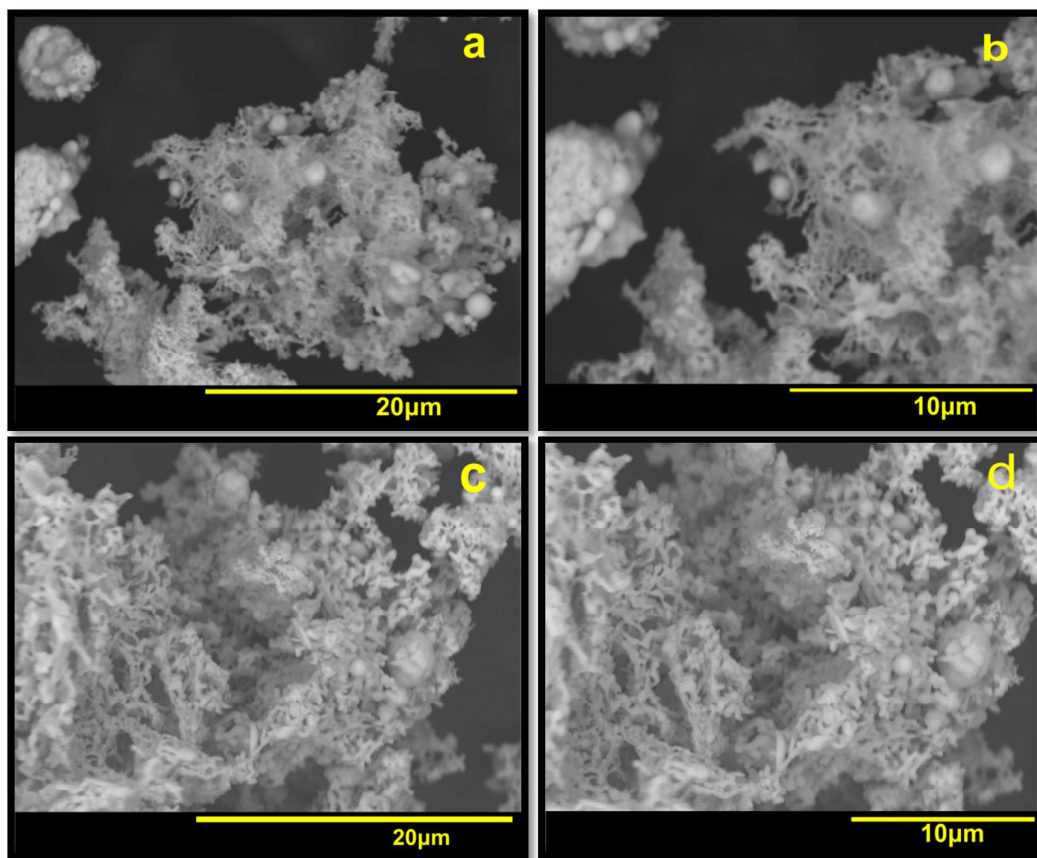


Fig. 2.



**Fig. 3.**

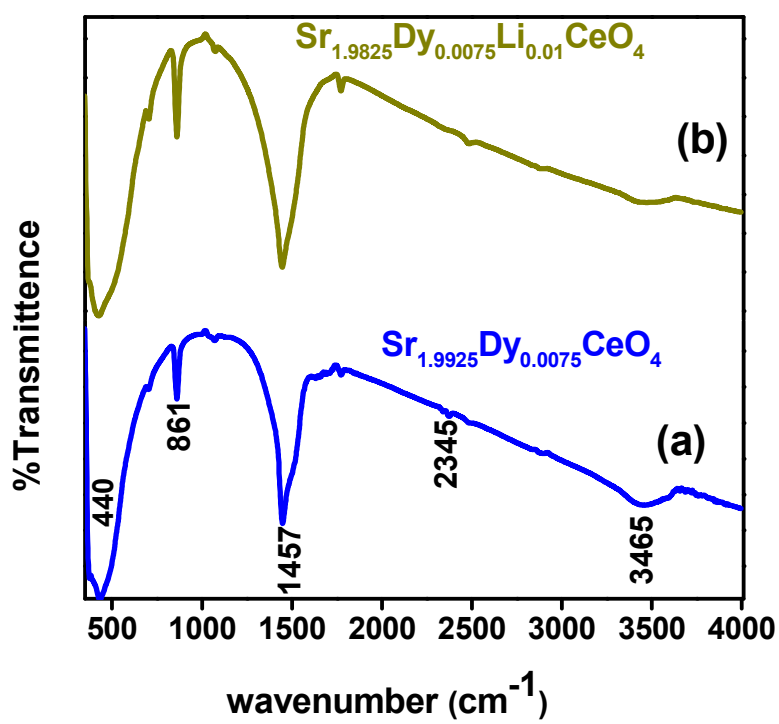


Fig. 4.

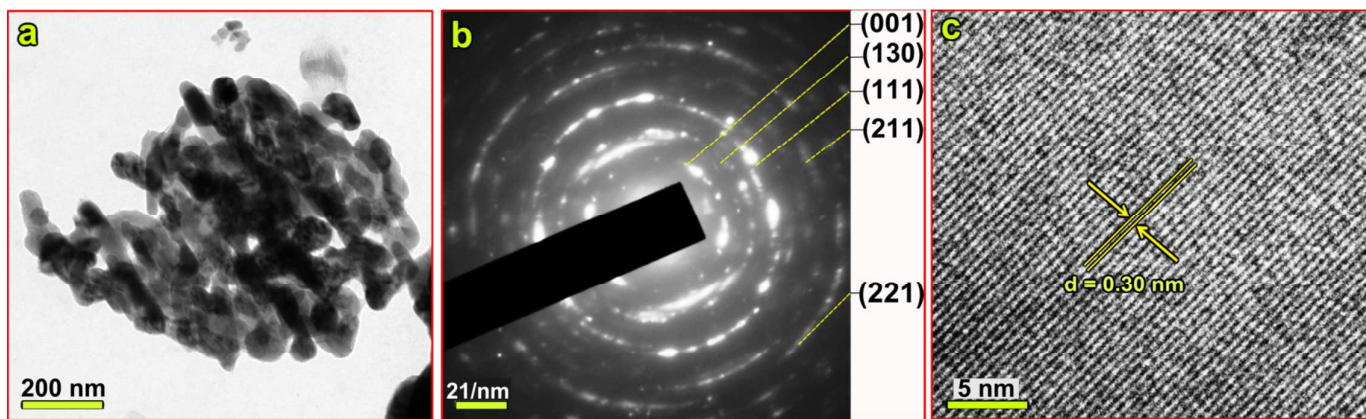


Fig. 5.

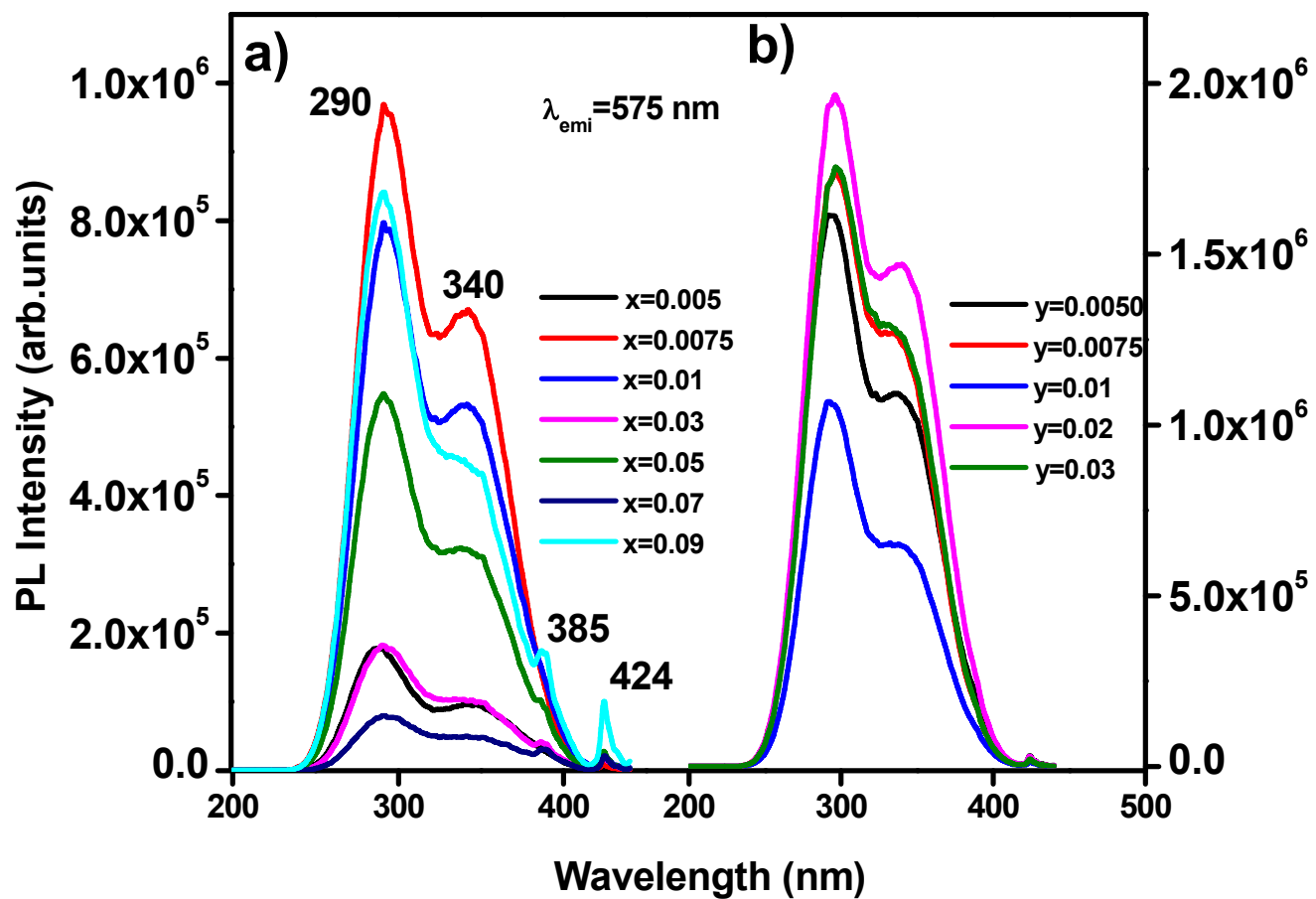


Fig. 6.

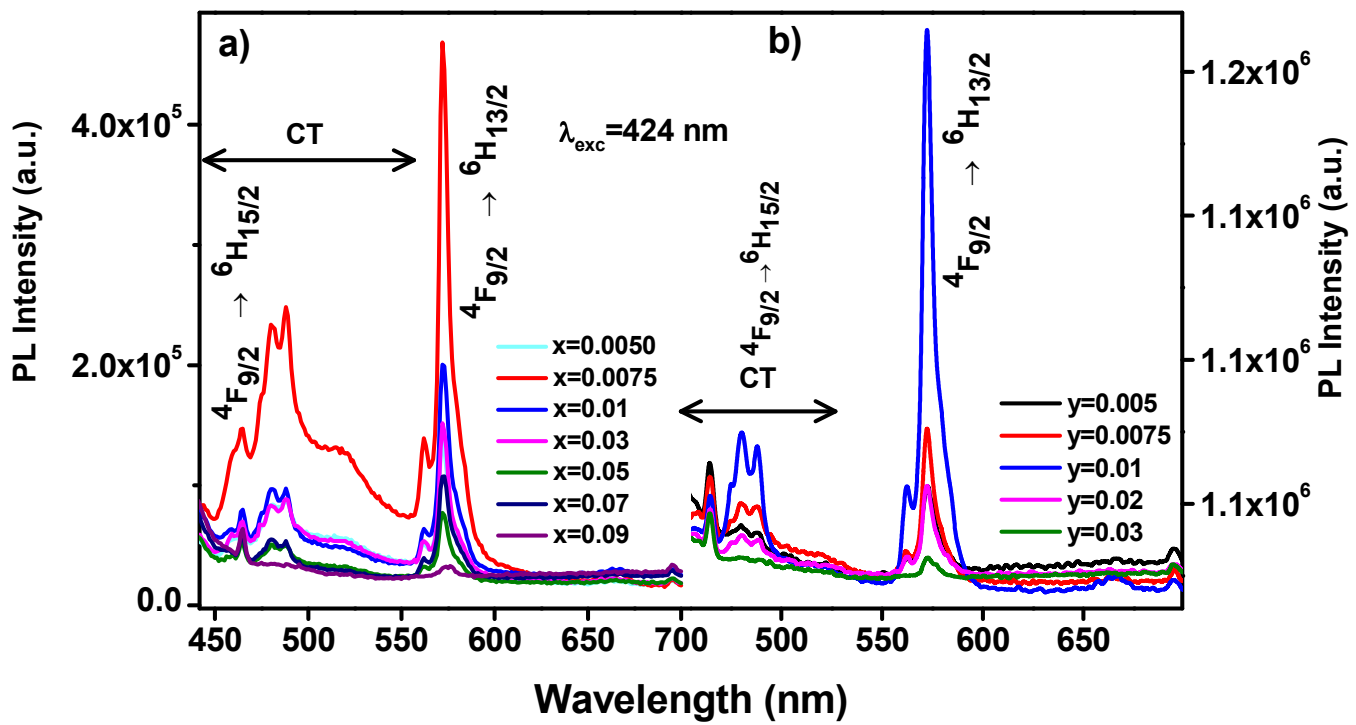


Fig.7.

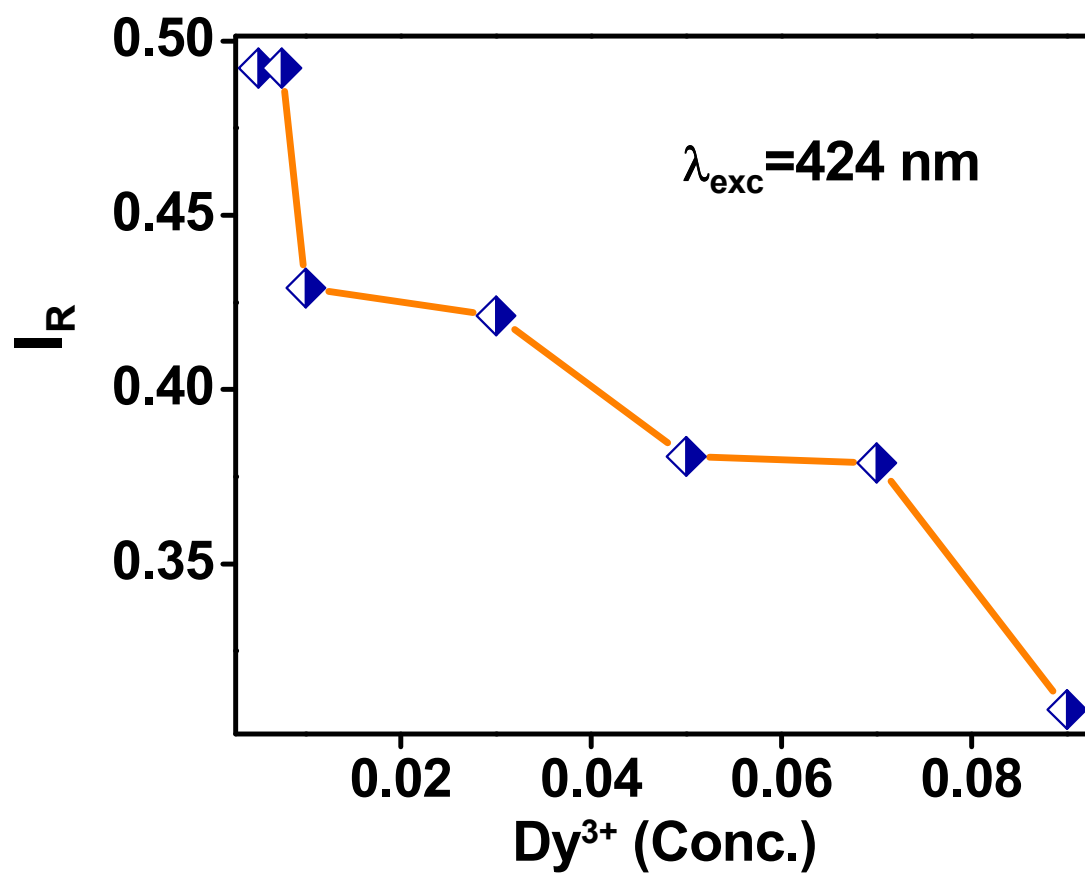


Fig. 8.

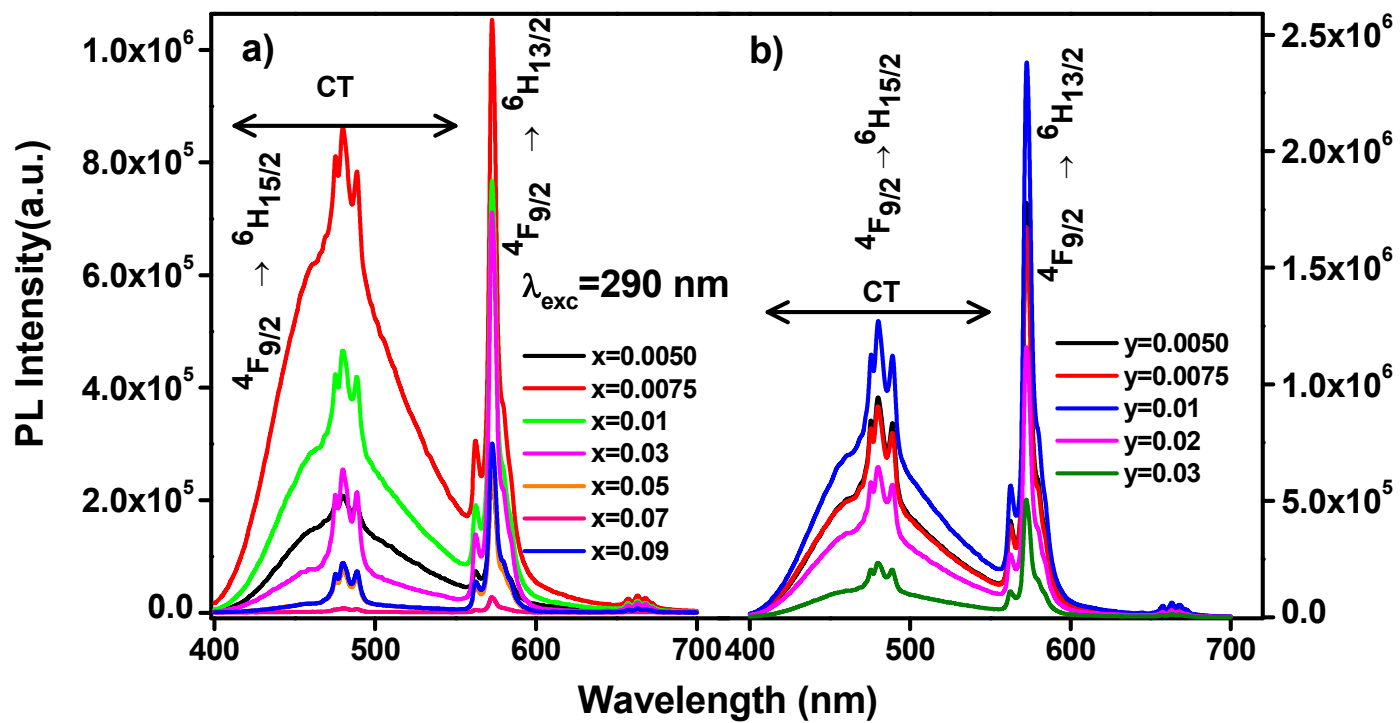


Fig.9.

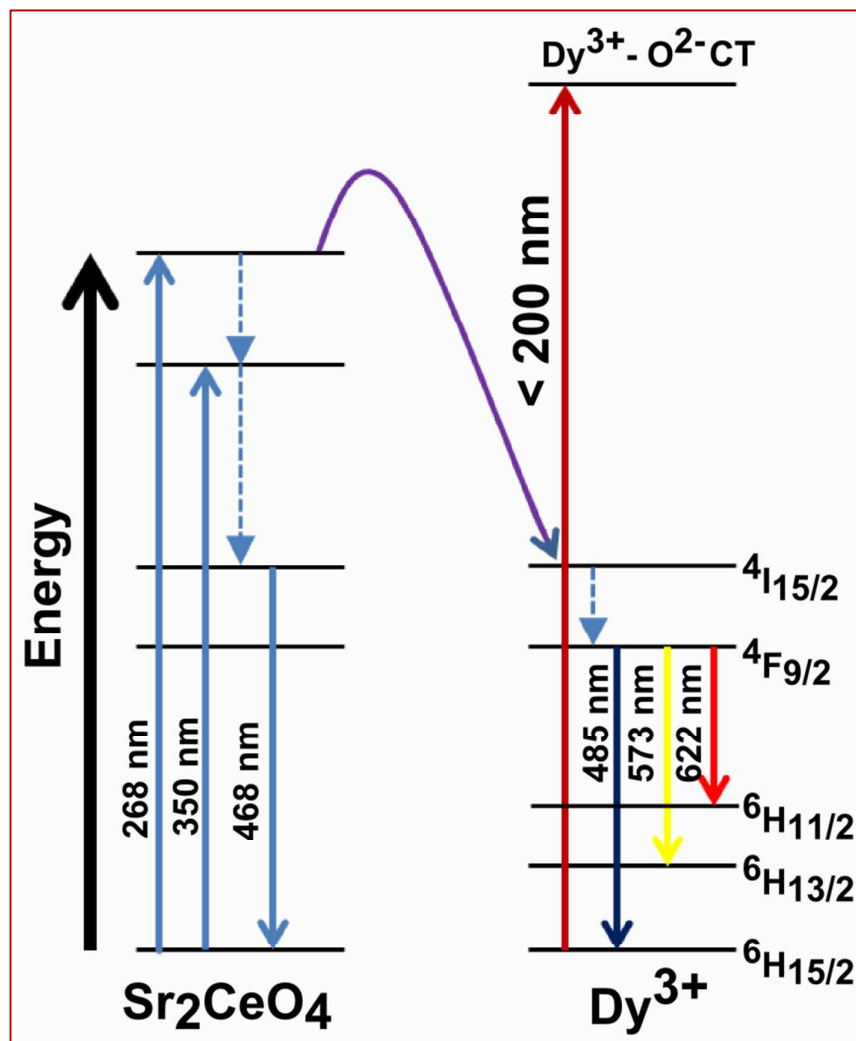


Fig. 10.

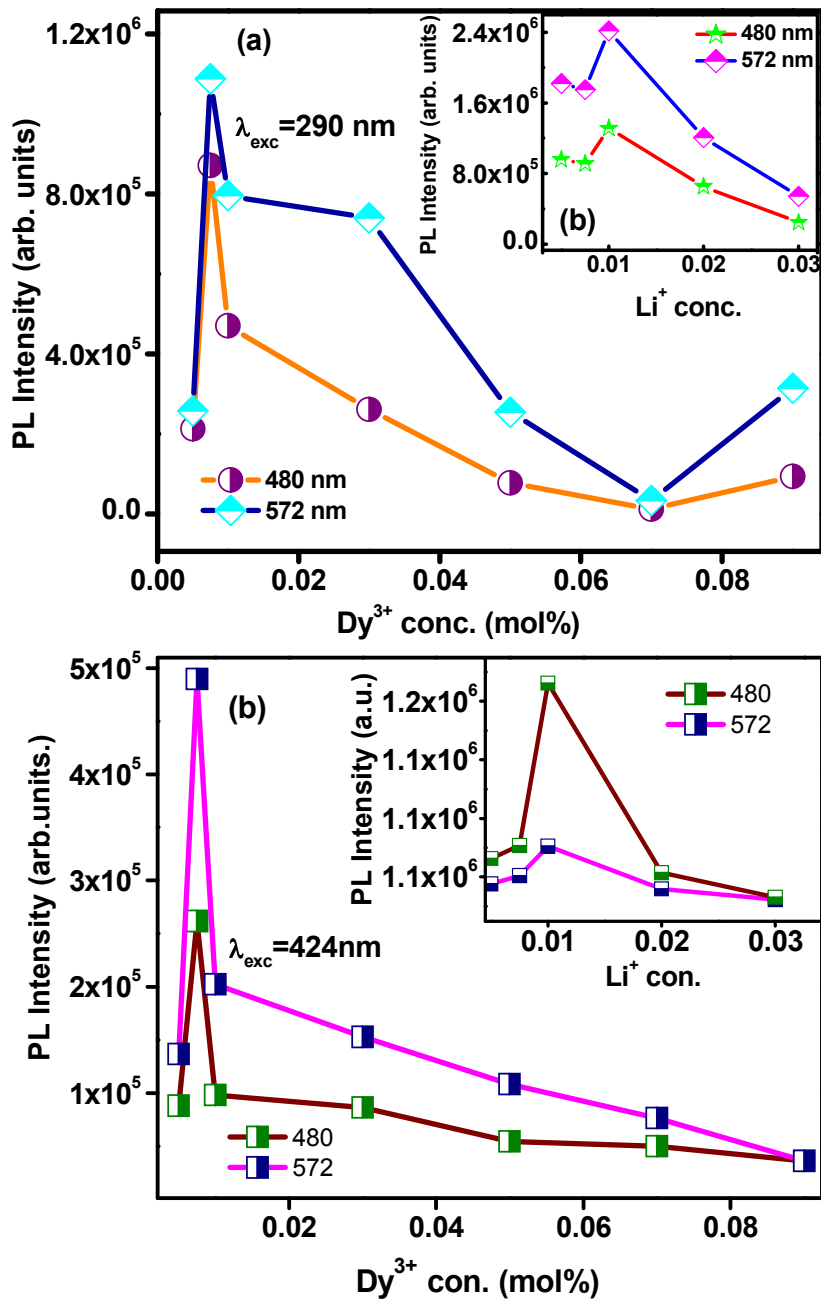


Fig.11

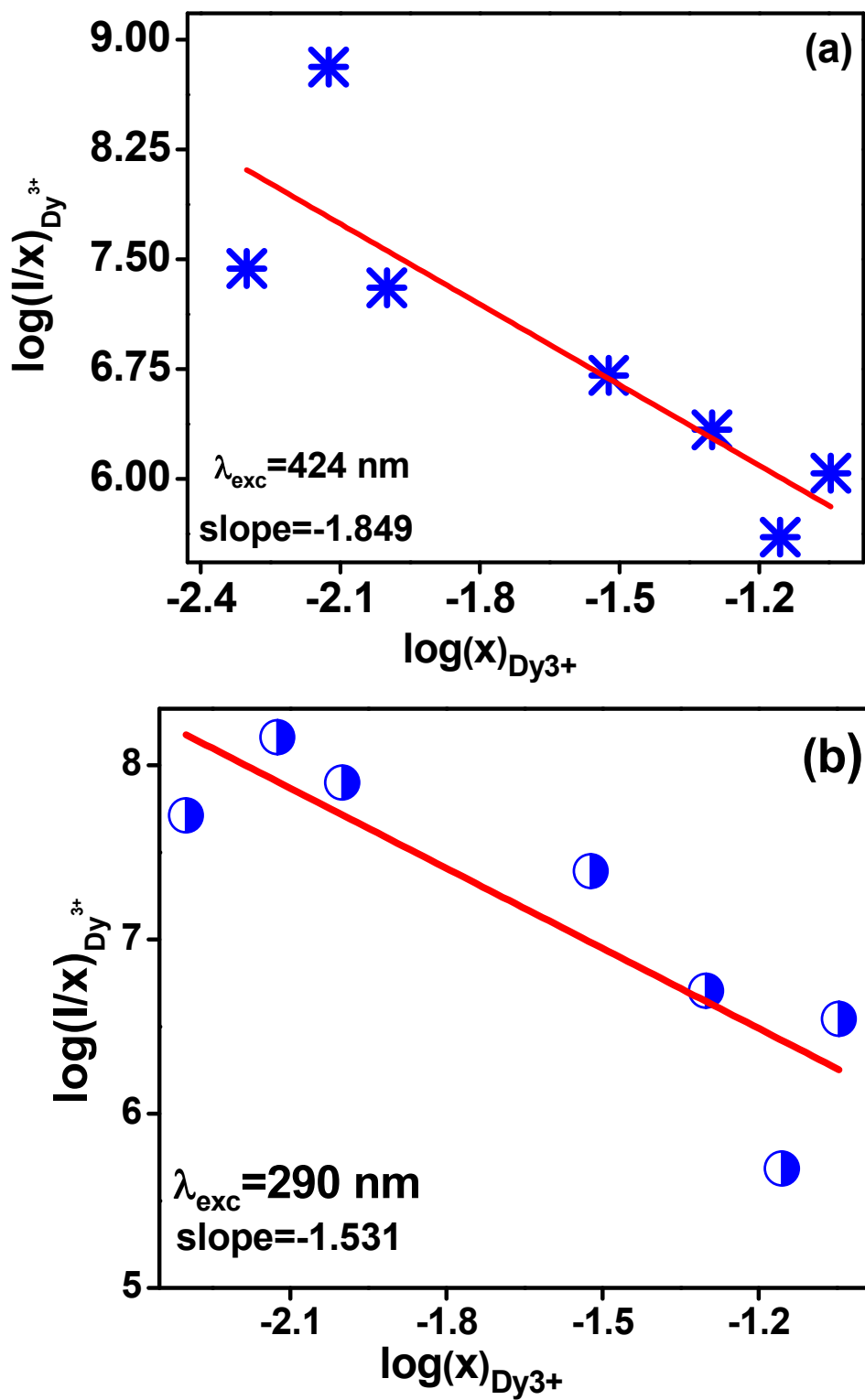


Fig.12

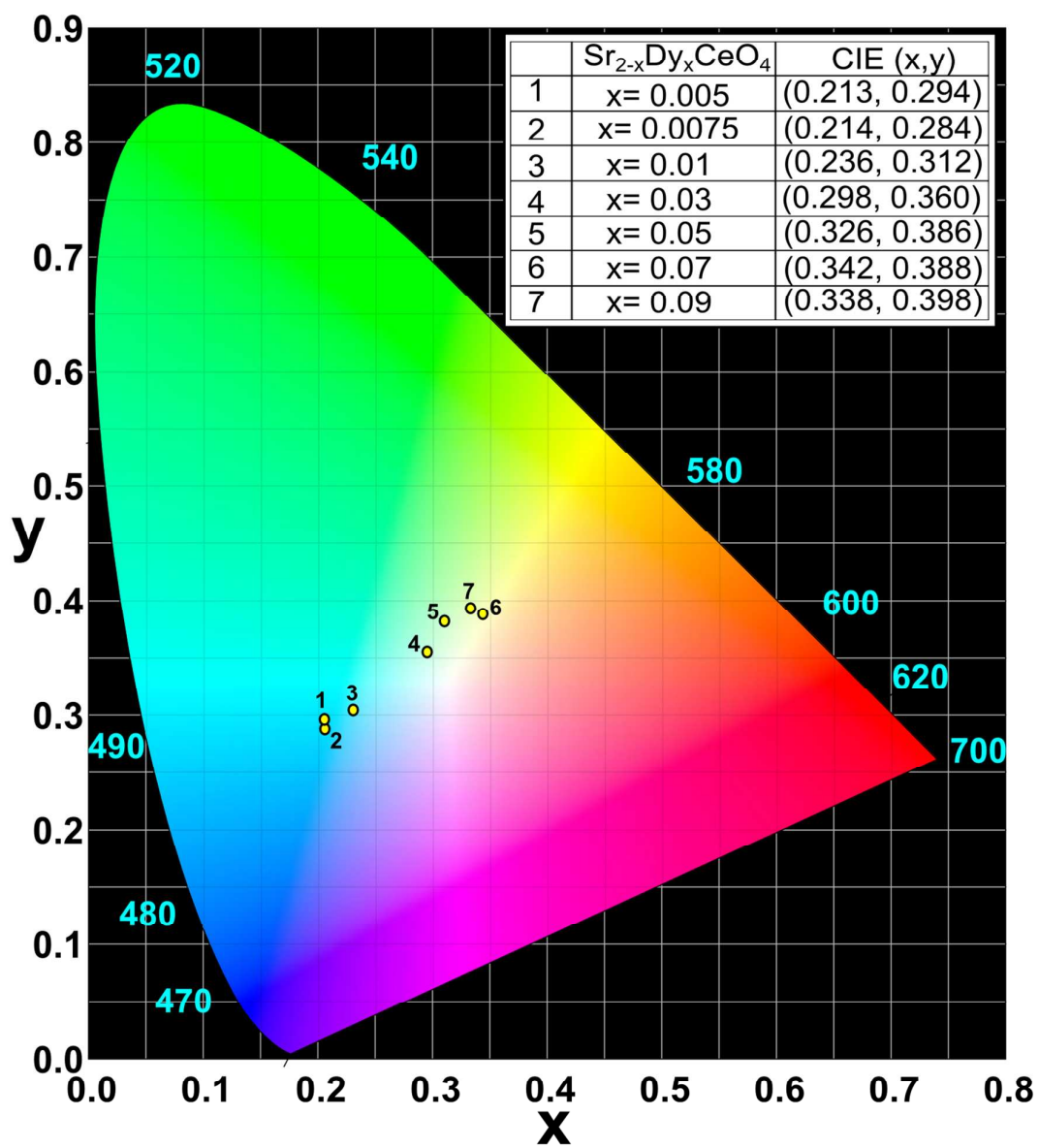


Fig.13

**Table:1**

Dy <sup>3+</sup> Conc.	Lattice parameter (Å)			V Å <sup>3</sup>	D nm	Li <sup>+</sup> Conc.	Lattice parameter (Å)			V Å <sup>3</sup>	D nm
	a b c						a b c				
	a	b	c				a	b	c		
0.005	6.10	1.05	3.59	230.0	28.0	0.005	6.10	1.05	3.58	228.0	27.0
0.0075	6.10	1.05	3.60	230.0	24.0	0.0075	6.10	1.050	3.60	228.5	27.0
0.01	6.06	1.05	3.60	229.5	23.0	0.01	6.10	1.05	3.60	229.0	32.0
0.03	6.06	1.05	3.60	229.5	18.0	0.02	6.10	1.04	3.58	229.0	27.0
0.05	6.06	1.05	3.60	229.2	22.0	0.03	6.10	1.04	3.58	227.0	25.0
0.07	6.05	1.05	3.61	229.0	19.0						
0.09	6.05	1.05	3.66	229.0	19.0						